

An asynchronous parallel high-throughput model calibration framework for crystal plasticity finite element constitutive models

Anh Tran^{1*} and Hojun Lim²

^{1*}Scientific Machine Learning, Sandia National Laboratories, Albuquerque, NM, 87123, USA.

²Computational Materials & Data Science, Sandia National Laboratories, Albuquerque, NM, 87123, USA.

*Corresponding author(s). E-mail(s): anhtran@sandia.gov;
Contributing authors: hnlm@sandia.gov;

Abstract

Crystal plasticity finite element model (CPFEM) is a powerful numerical simulation in the integrated computational materials engineering (ICME) toolboxes that relates microstructures to homogenized materials properties and establishes the structure-property linkages in computational materials science. However, to establish the predictive capability, one needs to calibrate the underlying constitutive model, verify the solution and validate the model prediction against experimental data. Bayesian optimization (BO) has stood out as a gradient-free efficient global optimization algorithm that is capable of calibrating constitutive models for CPFEM. In this paper, we apply a recently developed asynchronous parallel constrained BO algorithm to calibrate phenomenological constitutive models for stainless steel 304L, Tantalum, and Cantor high-entropy alloy.

Keywords: Bayesian optimization, inverse problem, constitutive model calibration, crystal plasticity finite element, 304L stainless steel, Tantalum, Cantor alloy

1 Introduction

Researching and developing predictive integrated computational materials engineering (ICME) models at multiple length-scales and time-scales has been conducted at the last two decades. In order to establish the predictive capability, the ICME model must be numerically verified and experimentally validated, in the spirit of uncertainty quantification. The development of ICME models as the third paradigm and scientific machine learning as the fourth paradigm [1, 2] is consistent with the Materials Genome Initiative [3–5], which has long been held as a cornerstone in materials science.

In the ICME context, crystal plasticity finite element model (CPFEM), along with phase-field simulations, have been the main workhorses of computational materials science to investigate the structure-property relationship. By targeting the mesoscale, which is sandwiched between microscale and macroscale, they are also important toolboxes in tackling multiscale ICME models. Numerous constitutive models have been proposed over the past few decades, including but not limited to [6], isotropic J_2 plasticity, phenomenological crystal plasticity, dislocation-density-based crystal plasticity, atomistically-informed crystal plasticity, crystal plasticity including dislocation flux. Depending on the materials system of interest and its corresponding crystal structures, as well as the parameterization of the constitutive model used, there are many parameters underpinning the constitutive model that one may need to calibrate against a suitable experimental setup.

Constitutive model calibration has been fairly well-studied within the literature. Loosely speaking, calibrating a constitutive model for CPFEM can be formulated as an optimization problem, which in turn minimizes the misfit between the CPFEM and experimental data. However, most approaches, if not all as of this point, mainly utilized sequential optimization, which suffers from the high computational cost of the forward CPFEM model. Even though the high computational cost can be somewhat mitigated by message passing interface (MPI) parallelism on multi-core high-performance computers, it also follows a diminishing return characterized by Amdahl’s law [7]. Modern optimization approaches often exploit both MPI (or MPI+X for heterogeneous) parallelism as well as optimization parallelism on high-performance computers and are capable of delivering a better solution in shorter wallclock time. Compared to sequential optimization approaches, parallel optimization approaches can offer better performance in calibrating ICME models, especially for prototyping models that do not scale well with multi-cores and multi-threads on high-performance computing platforms.

Since the birth of CPFEM [8–11], there have been numerous works in the literature dedicated to calibrating constitutive model in many materials system. Due to limited space, we attempt to review some notable works that are relevant to constitutive model calibration in the context of CPFEM. Chakraborty and Eisenlohr [12] proposed a modified Nelder–Mead optimization algorithm to treat the objective function when evaluation fails and demonstrated their algorithm on the single crystal nano-indentation for face-centered

cubic materials systems. Hérault et al. [13] applied the Levenberg-Marquadt gradient-based optimization algorithm to calibrate an isotropic constitutive model for dual phase steel DP600. Nguyen et al. [14] applied Markov chain Monte Carlo on top of a Gaussian process (GP) regression to obtain a posterior of a dislocation-density-based constitutive model parameters for copper. Savage et al. [15] applied genetic algorithm multi-objective optimization algorithm to calibrate a dislocation-density-based constitutive model for dual phase 780 steel against multiple criteria. Hochhalter et al. [16] applied the Nelder–Mead and Broyden–Fletcher–Goldfarb–Shanno optimization algorithms before running Markov Chain Monte Carlo to obtain the posterior of a phenomenological constitutive model parameters for aluminum oligocrystal. Kuhn et al. [17] also utilized Bayesian optimization (BO) to calibrate a phenomenological constitutive model for 50CrMo4 steel. Sedighiani et al. [18, 19] applied genetic algorithm to calibrate both phenomenological and dislocation-density-based constitutive models for face-centered cubic copper, body-centered cubic steel, and hexagonal-close packed magnesium. Wang et al. [20] employed the gradient-based least-squares optimization algorithm to calibrate a micropolar plasticity in Hostun sand. Liu et al. [21] employed a Gauss–Newton trust region optimization algorithm to calibrate a phenomenological Dafalias–Manzari constitutive model for Nevada sand. Herrera-Solaz et al. [22] used the Levenberg–Marquadt optimization algorithm to calibrate a phenomenological constitutive model for AZ31 Magnesium alloy. Do and Ohsaki [23, 24] proposed a multi-objective BO to calibrate an elastoplastic constitutive model for a structural steel. Seidl and Granzow [25] proposed an automatic differentiation framework to calibrate parameters in elastoplastic constitutive model. Corona et al. [26] calibrated three yield functions, von Mises, Hill-48, and Yld2004-18p on a 7079 aluminum alloy against digital image correlation experimental data, which were subsequently verified and validated in Jones et al [27]. Karandikar et al. [28] also applied BO to calibrate a Johnson-Cook flow stress model. Sun and Wang [29] applied BO to calibrate a Voce hardening law for Magnesium alloy ZEK100 in a viscoplastic self-consistent polycrystal plasticity model with twinning and de-twinning scheme. Morand and Helm [30] utilized a mixture of experts with an ensemble of neural networks to calibrate an exponential hardening model. Generale et al. [31] applied parallel MCMC to calibrate a viscous multimode damage model in an oxide-oxide ceramic matrix composite. Zambaldi et al. [32] applied the Nelder–Mead optimization algorithm to calibrate a phenomenological constitutive model for α Titanium. Bolzon et al. [33] applied the trust region optimization algorithm to calibrate an elastoplastic constitutive model for ductile metals. Fuhg et al. utilized the partially convex neural network [34] and local GP [35] to derive a data-driven macroscopic yield function. Zhang et al. [36] calibrated a Johnson-Cook constitutive model in advanced high strength steel DP1180 against nano-indentation experimental data. Foumani et al. [37] proposed a multi-fidelity BO approach based on latent map GP and applied on nanolaminate ternary alloy family as well as organic-inorganic perovskite datasets. Wang et al. [38] proposed a q-EI

algorithm to parallelize BO in an asynchronous manner and analyzed the convergence accordingly. Veasna et al. [39] proposed to couple SMS-EGO [40], which is a hypervolume-based approach, to calibrate constitutive model for elasto-plastic self-consistent CPFEM model. Bostanabad et al. [41] incorporated and optimized the nugget parameter as an additional hyperparameter for noisy environment, such as experimental observations.

Despite the fact that numerous constitutive model calibration works have been done in the literature, not too many have taken a parallel optimization route that offers greater efficiency in terms of computational cost. In this paper, we apply a recently developed asynchronous parallel constrained BO algorithm [42], built upon the GP-Hedge algorithm [43], to calibrate phenomenological constitutive models for stainless steel 304L, Tantalum, and Cantor high-entropy alloy. Compared to other previous works listed above, one of the significant advantages of this framework is the asynchronous parallel feature, which allows multiple CPFEM simulations running asynchronous parallel on high-performance computers to optimize the objective in shorter wallclock time.

The remainder of the this paper is organized as follows. Section 2 introduces the BO algorithm used in this paper, its underlying GP and the adaptive sampling strategy for finding the next query point. Section 3 describes the phenomenological constitutive model, based on the open-source DAMASK CPFEM package [6]. Section 4 introduces the asynchronous parallel constitutive model calibration workflow used in this paper. Section 5 describes the numerical and experimental results for stainless steel 304L. Section 6 describes the numerical and experimental results for Tantalum. Section 7 describes the numerical and experimental results for Cantor high-entropy alloy. Section 8 discusses and concludes the paper.

2 Bayesian optimization

In this section, we introduce the BO concept, which is based on GP and an asynchronous parallel sampling strategy that allows multiple acquisition functions simultaneously.

2.1 Gaussian process regression and Bayesian optimization

Comprehensive and critical review studies are provided by Brochu et al. [44], Shahriari et al. [45], Frazier [46], and Jones et al. [47] for BO method and its variants. We adopt the notation from Shahriari et al. [45] and Tran et al. [42, 48–54]. In this formulation, we treat the optimization problem in the maximization setting,

$$\mathbf{x}^* = \operatorname{argmax}_{\mathbf{x} \in \mathcal{X}} f(\mathbf{x}) \quad (1)$$

subject to a set of nonlinear inequalities constraints $\lambda_j(\mathbf{x}) \leq 0$, $1 \leq j \leq J$, assuming that f is a function of \mathbf{x} , where $\mathbf{x} \in \mathcal{X} \subset \mathbb{R}^d$ is the d -dimensional

input. A $\mathcal{GP}(\mu_0, k)$ is a non-parametric model over functions f , which is fully characterized by the prior mean functions $\mu_0(x) : \mathcal{X} \mapsto \mathbb{R}$ and the positive-definite kernel, or covariance function $k : \mathcal{X} \times \mathcal{X} \mapsto \mathbb{R}$.

Let the dataset $\mathcal{D} = (\mathbf{x}_i, y_i)_{i=1}^n$ denote a collection of n noisy observations. In GP regression, it is assumed that $\mathbf{f} = f_{1:n}$ is jointly Gaussian, and the observation y is normally distributed given f , leading to

$$\mathbf{f}|\mathbf{x} \sim \mathcal{N}(\mathbf{m}, \mathbf{K}), \quad (2)$$

$$\mathbf{y}|\mathbf{f}, \sigma^2 \sim \mathcal{N}(\mathbf{f}, \sigma^2 \mathbf{I}), \quad (3)$$

where $m_i := \mu(\mathbf{x}_i)$, and $K_{i,j} := k(\mathbf{x}_i, \mathbf{x}_j)$. Equation 2 describes the prior distribution induced by the GP.

The covariance kernel $k(\cdot, \cdot)$ is a choice of modeling covariance between inputs, depending on the smoothness assumption of f . The family of Matérn kernels is arguably one of the most popular choices for kernels, offering a broad class for stationary kernels which are controlled by a smoothness parameter $\nu > 0$ (cf. Section 4.2, [55]), including the square-exponential ($\nu \rightarrow \infty$) and exponential ($\nu = 1/2$) kernels. The Matérn kernels are described as

$$\mathbf{K}_{i,j} = k(\mathbf{x}_i, \mathbf{x}_j) = \theta_0^2 \frac{2^{1-\nu}}{\Gamma(\nu)} (\sqrt{2\nu}r)^\nu K_\nu(\sqrt{2\nu}r), \quad (4)$$

where K_ν is a modified Bessel function of the second kind and order ν . Common kernels for GP include [45]

- $\nu = 1/2$: $k_{\text{Matérn}1/2}(\mathbf{x}, \mathbf{x}') = \theta_0^2 \exp(-r)$ (also known as exponential kernel),
- $\nu = 3/2$: $k_{\text{Matérn}3/2}(\mathbf{x}, \mathbf{x}') = \theta_0^2 \exp(-\sqrt{3}r)(1 + \sqrt{3}r)$,
- $\nu = 5/2$: $k_{\text{Matérn}5/2}(\mathbf{x}, \mathbf{x}') = \theta_0^2 \exp(-\sqrt{5}r) \left(1 + \sqrt{5}r + \frac{5}{3}r^2\right)$,
- $\nu \rightarrow \infty$: $k_{\text{sq-exp}}(\mathbf{x}, \mathbf{x}') = \theta_0^2 \exp\left(-\frac{r^2}{2}\right)$ (also known as square exponential or automatic relevance determination kernel),

where $r^2 = (\mathbf{x} - \mathbf{x}')^\top \mathbf{\Lambda} (\mathbf{x} - \mathbf{x}')$, and $\mathbf{\Lambda}$ is a diagonal matrix of d squared length scale θ_i .

Under the formulation of GP, given the dataset \mathcal{D}_n , the prediction for an unknown arbitrary point is characterized by the posterior Gaussian distribution, which can be described by the posterior mean and posterior variance functions, respectively as

$$\mu_n(\mathbf{x}) = \mu_0(\mathbf{x}) + \mathbf{k}(\mathbf{x})^\top (\mathbf{K} + \sigma^2 \mathbf{I})^{-1} (\mathbf{y} - \mathbf{m}), \quad (5)$$

and

$$\sigma_n^2(\mathbf{x}) = k(\mathbf{x}, \mathbf{x}) - \mathbf{k}(\mathbf{x})^\top (\mathbf{K} + \sigma^2 \mathbf{I})^{-1} \mathbf{k}(\mathbf{x}), \quad (6)$$

where $\mathbf{k}(\mathbf{x})$ is the covariance vector between the query point \mathbf{x} and $\mathbf{x}_{1:n}$. The main drawback of GP formulation is its scalability $\mathcal{O}(n^3)$ that originates from the computation of the inverse of the covariance matrix \mathbf{K} . Connection from GP to convolution neural network has been proposed where it is proved to be theoretically equivalent to single layer with infinite width [56] or infinite convolutional filters [57].

2.2 Acquisition function

In the traditional BO method, which is sequential, the GP model is constructed for the objective function, and the next sampling location is determined by maximizing the acquisition function based on the constructed GP. This acquisition function is evaluated based on the underlying GP surrogate model, thus converting the cost of evaluating the real simulation to the cost of evaluating on the GP model. The latter is much more computationally appealing because it is semi-analytical. The acquisition function must balance between the exploitation and exploration flavors of the BO method. Too much exploitation would drive the numerical solution to a local minima, whereas too much exploration would make BO an inefficient optimization method. We review three main acquisition functions that are typically used in the literature: the probability of improvement (PI), the expected improvement (EI), and the upper confidence bounds (UCB).

Denote $\mu(\mathbf{x})$, $\sigma^2(\mathbf{x})$, and θ as the posterior mean, the posterior variance, and the hyper-parameters of the objective GP model, respectively. θ is obtained by maximizing the log likelihood estimation over a plausible chosen range, where the likelihood is described as

$$\begin{aligned} \log p(\mathbf{y}|\mathbf{x}_{1:n}, \theta) &= -\frac{n}{2} \log(2\pi) \\ &\quad - \frac{1}{2} \log |\mathbf{K}^\theta + \sigma^2 \mathbf{I}| \\ &\quad - \frac{1}{2} (\mathbf{y} - \mathbf{m}_\theta)^T (\mathbf{K}^\theta + \sigma^2 \mathbf{I})^{-1} (\mathbf{y} - \mathbf{m}_\theta). \end{aligned} \quad (7)$$

Let $\phi(\cdot)$ and $\Phi(\cdot)$ be the standard normal probability distribution function and cumulative distribution function, respectively, and $\mathbf{x}_{\text{best}} = \underset{1 \leq i \leq n}{\operatorname{argmax}} f(\mathbf{x}_i)$ be the best-so-far sample. Rigorously, the acquisition function should be written as $\alpha(\mathbf{x}; \{\mathbf{x}_i, y_i\}_{i=1}^n, \theta)$, but for the sake of simplicity, we drop the dependence on the observations and simply write as $\alpha(\mathbf{x})$ and $\mathbb{E}(\cdot)$ is implicitly understood as $\mathbb{E}_{y \sim p(y|\mathcal{D}_n, \mathbf{x})}(\cdot)$ unless specified otherwise.

The PI acquisition function [58] is defined as

$$\alpha_{\text{PI}}(\mathbf{x}) = \Pr(y > f(\mathbf{x}_{\text{best}})) = \mathbb{E}[\mathbb{1}_{y > f(\mathbf{x}_{\text{best}})}] = \Phi(\gamma(\mathbf{x})), \quad (8)$$

where

$$\gamma(\mathbf{x}) = \frac{\mu(\mathbf{x}) - f(\mathbf{x}_{\text{best}})}{\sigma(\mathbf{x})}, \quad (9)$$

indicates the deviation away from the best sample. The PI acquisition function is constructed based on the idea of binary utility function, where a unit reward is received if a new best-so-far sample is found, and zero otherwise.

The EI acquisition function [59–63] is defined as

$$\alpha_{\text{EI}}(\mathbf{x}) = \sigma(\mathbf{x}) [\gamma(\mathbf{x})\Phi(\gamma(\mathbf{x})) + \phi(\gamma(\mathbf{x}))]. \quad (10)$$

The EI acquisition is constructed based on an improvement utility function, where the reward is the relative difference if a new best-so-far sample is found, and zero otherwise. A closely related generalization of the EI acquisition function, called knowledge-gradient (KG) acquisition function, has been suggested in [64]. Under the assumptions of noise-free and the sampling function is restricted, the EI acquisition function is recovered from the KG acquisition function. If the EI acquisition function is rewritten as

$$\begin{aligned} \alpha_{\text{EI}}(\mathbf{x}) &= \mathbb{E} [\max(y, f(\mathbf{x}_{\text{best}})) - f(\mathbf{x}_{\text{best}})] \\ &= \mathbb{E} [\max(y - f(\mathbf{x}_{\text{best}}), 0)] \\ &= \mathbb{E} [(y - f(\mathbf{x}_{\text{best}}))^+], \end{aligned} \quad (11)$$

then the KG acquisition function is expressed as

$$\alpha_{\text{KG}}(\mathbf{x}) = \mathbb{E} [\max \mu_{n+1}(\mathbf{x}) | \mathbf{x}_{n+1} = \mathbf{x}] - \max(\mu_n(\mathbf{x})) \quad (12)$$

for one-step look-ahead acquisition function.

The UCB acquisition function [65–67] is defined as

$$\alpha_{\text{UCB}}(\mathbf{x}) = \mu(\mathbf{x}) + \kappa\sigma(\mathbf{x}), \quad (13)$$

where κ is a hyper-parameter describing the acquisition exploitation-exploration balance. Here, we adopt the κ computation from Daniel et al. [68], where

$$\kappa = \sqrt{\nu\gamma_n}, \quad \nu = 1, \quad \gamma_n = 2 \log \left(\frac{n^{d/2+2} \pi^2}{3\delta} \right), \quad (14)$$

and d is the dimensionality of the problem, and $\delta \in (0, 1)$ [67].

Another type acquisition function is entropy-based, such as GP-PES [69–72], GP-ES [73], GP-MES [74]. Since the GP is collectively a distribution of functions, the distribution of the global optimum \mathbf{x}^* can be estimated as well from sampling the GP posterior. The predictive-entropy-search (PES) [69] can be written in terms of the differential entropy $H(\cdot)$ as

$$\begin{aligned} \alpha_{\text{PES}}(\mathbf{x}) &= H[p(\mathbf{x}^* | \mathcal{D}_n)] - \mathbb{E} [H[p(\mathbf{x}^* | \mathcal{D} \cup \{(\mathbf{x}, y)\})]] \\ &= H[p(y | \mathcal{D}_n, \mathbf{x})] - \mathbb{E}_{p(\mathbf{x}^* | \mathcal{D}_n)} [H(p(y | \mathcal{D}_n, \mathbf{x}, \mathbf{x}^*))] \end{aligned} \quad (15)$$

Wang et al. [74] proposed GP-MES acquisition function, which effectively suggests sampling y^* from the 1-dimensional output space \mathbb{R} using Gumbel

Table 1: $1^{+/-}$: right-/left-continuous Heaviside step function; ReLU + sigmoid (σ) + softmax: activation function; $\Sigma = \mathbf{L}\mathbf{L}^\top$: Cholesky factorization; $\gamma \sim \mathcal{N}(\mathbf{0}, \Sigma)$ residual

Abbr.	Acquisition function \mathcal{L}	Reparameterization
EI	$\mathbb{E}_{\mathbf{y}}[\max(\text{ReLU}(\mathbf{y} - \alpha))]$	$\mathbb{E}_{\mathbf{z}}[\max(\text{ReLU}(\mu + \mathbf{Lz} - \alpha))]$
PI	$\mathbb{E}_{\mathbf{y}}[\max(1^-(\mathbf{y} - \alpha))]$	$\mathbb{E}_{\mathbf{z}}[\max(\sigma(\frac{\mu + \mathbf{Lz} - \alpha}{\tau}))]$
SR	$\mathbb{E}_{\mathbf{y}}[\max(\mathbf{y})]$	$\mathbb{E}_{\mathbf{z}}[\max(\mu + \mathbf{Lz})]$
UCB	$\mathbb{E}_{\mathbf{y}}[\max(\mu + \sqrt{\frac{\beta\pi}{2}} \mathbf{y})]$	$\mathbb{E}_{\mathbf{z}}[\max(\mu + \sqrt{\frac{\beta\pi}{2}} \mathbf{Lz})]$
ES	$-\mathbb{E}_{\mathbf{y}_a}[\mathbb{H}(\mathbb{E}_{\mathbf{y}_b \mathbf{y}_a}[1^+(\mathbf{y}_b - \max(\mathbf{y}_b))])]$	$-\mathbb{E}_{\mathbf{z}_a}[\mathbb{H}(\mathbb{E}_{\mathbf{z}_b}[\text{softmax}(\frac{\mu_{b a} + \mathbf{L}_{b a}\mathbf{z}_b}{\tau})])]$
KG	$\mathbb{E}_{\mathbf{y}_a}[\max(\mu_b + \Sigma_{b,a}\Sigma_{a,a}^{-1}(\mathbf{y}_a - \mu_a))]$	$\mathbb{E}_{\mathbf{z}_a}[\max(\mu_b + \Sigma_{b,a}\Sigma_{a,a}^{-1}\mathbf{L}_a\mathbf{z}_a)]$

distribution instead of \mathbf{x} in the high-dimensional input space \mathcal{X} , i.e.

$$\alpha_{\text{MES}}(\mathbf{x}) = H[p(\mathbf{y}|\mathcal{D}_n, \mathbf{x})] - \mathbb{E}[H(p(\mathbf{y}|\mathcal{D}_n, \mathbf{x}, \mathbf{y}^*))], \quad (16)$$

Last but not least, since $f(\mathbf{x})$ is Gaussian, the differential entropy can be simplified to a function of posterior variance $\sigma^2(\mathbf{x})$, i.e.

$$H[p(\mathbf{y}|\mathcal{D}_n, \mathbf{x})] = 0.5 \log [2\pi e(\sigma^2(\mathbf{x}) + \sigma^2)], \quad (17)$$

and thus pure exploration search which targets \mathbf{x} with maximum posterior variance $\sigma^2(\mathbf{x})$, i.e. $\alpha_{\text{PE}}(\mathbf{x}) = \sigma^2(\mathbf{x})$ is theoretically identical with the maximum differential entropy [69]. Interestingly, Wilson et al. [75] proposed a reparameterization of most commonly used acquisition functions in terms of deep learning convolution kernels. Wilson [75] presented a reparameterization scheme for different acquisition functions in term of activation function for neural networks, summarizing in the following table.

2.3 Constraints

A review and comparison study is performed by Parr et al. [76] for different schemes to handle constraints using both synthetic and real-world applications. Many previous works discussed below in the literature prefer to couple constraint satisfaction problems with the EI acquisition due to its consistent numerical performance. Even though constraints can be classified to many types, for example [77], known versus unknown, quantifiable versus nonquantifiable, a priori versus simulation, relaxable versus unrelaxable, in this work, we mainly focus on two types of constraints, namely known and unknown. Known constraints, which are typically physics-based, do not require to invoke the functional evaluation and are often computationally cheap. We model known constraints by penalizing the acquisition function with an indicator function $\mathbb{I}(\mathbf{x})$, depending on whether constraints are violated.

$$\alpha_{\text{constrained}}^{\text{known}}(\mathbf{x}) = \alpha(\mathbf{x})\mathbb{I}_{\text{known}}(\mathbf{x}), \quad (18)$$

where

$$\mathbb{I}_{\text{known}}(\mathbf{x}) = \begin{cases} 1, & \lambda(\mathbf{x}) \leq \mathbf{c} \\ 0, & \lambda(\mathbf{x}) \not\leq \mathbf{c} \end{cases} \quad (19)$$

Unknown or hidden constraints usually occurs when outputs of a forward computational model is *NaN* or *Inf*. For such cases, we augment the probability of failure by a binary probabilistic classifier into the acquisition function in a soft penalization manner as

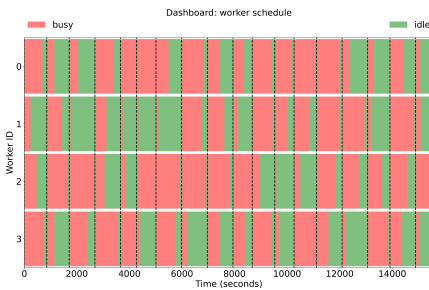
$$\alpha_{\text{constrained}}^{\text{unknown}}(\mathbf{x}) = \begin{cases} \alpha(\mathbf{x}), & \text{with } \Pr(\text{clf}(\mathbf{x}) = 1), \\ 0, & \text{with } \Pr(\text{clf}(\mathbf{x}) = 0). \end{cases} \quad (20)$$

The expected acquisition function, therefore, follows as

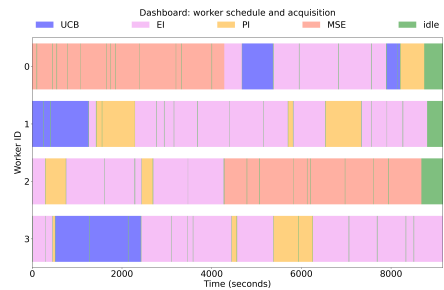
$$\mathbb{E}[\alpha_{\text{constrained}}^{\text{unknown}}(\mathbf{x})] = \alpha(\mathbf{x})\Pr_{\text{unknown}}(\text{clf}(\mathbf{x}) = 1). \quad (21)$$

2.4 Asynchronous parallel

We adopt the GP-Hedge scheme [78] to sample a portfolio of acquisition functions according to their rewards. The main idea of GP-Hedge is to adaptively select a suitable acquisition function, whether it is EI, PI, UCB, or something else, depending their overall performance with respect to the optimization objective. Figure 1 compares between the batch-sequential parallelism versus the asynchronous parallelism. It can be observed that if the randomness of the application runtime is significant, employing an asynchronous parallel approach may lead to a substantial reduction in wallclock time, assuming there is sufficient computational resource.



(a) Batch-sequential parallel BO [51].



(b) Asynchronous parallel BO [42].

Fig. 1: Comparison between batch parallel BO [51] and asynchronous parallel BO [42] showing a substantial improvement in wallclock time reduction. By aggressively targeting the idle time for concurrent workers on high-performance computers, the wallclock time can reduce significantly. The actual improvement in wallclock time depends mainly on the stochasticity in real runtime of the application of interest.

3 Crystal plasticity finite element with phenomenological constitutive model

A phenomenological crystal plasticity constitutive model used for face-centered cubic (FCC) crystals was first proposed by Hutchinson [79] and extended for deformation twinning by Kalidindi [80]. The plastic component is parameterized in terms of resistance ξ on N_s slip and N_{tw} twin systems. The resistances on $\alpha = 1, \dots, N_s$ slip systems evolve from ξ_0 to a system-dependent saturation value and depend on shear on slip and twin systems according to

$$\begin{aligned} \dot{\xi}^\alpha &= h_0^{s-s} \left[1 + c_1 \left(f_{tw}^{tot} \right)^{c_2} \right] \left(1 + h_{int}^\alpha \left[\sum_{\alpha'=1}^{N_s} |\dot{\gamma}^{\alpha'}| \left| 1 - \frac{\xi^{\alpha'}}{\xi_\infty^{\alpha'}} \right|^a \operatorname{sgn} \left(1 - \frac{\xi^{\alpha'}}{\xi_\infty^{\alpha'}} \right) h^{\alpha\alpha'} \right] \right) \\ &+ \sum_{\beta'=1}^{N_{tw}} \dot{\gamma}^{\beta'} h^{\alpha\beta'}, \end{aligned} \quad (22)$$

where f_{tw}^{tot} is the total twin volume fraction, h denotes the components of the slip-slip and slip-twin interaction matrices, h_0^{s-s} , h_{int} , c_1 , c_2 are model-specific fitting parameters and ξ_∞ represents the saturated resistance.

The resistances on the $\beta = 1, \dots, N_{tw}$ twin systems evolve in a similar way,

$$\dot{\xi}^\beta = h_0^{tw-s} \left(\sum_{\alpha=1}^{N_s} |\dot{\gamma}^\alpha| \right)^{c_3} \left(\sum_{\alpha'=1}^{N_s} |\dot{\gamma}^{\alpha'}| h^{\beta\alpha'} \right) + h_0^{tw-tw} \left(f_{tw}^{tot} \right)^{c_4} \left(\sum_{\beta'=1}^{N_{tw}} \dot{\gamma}^{\beta'} h^{\beta\beta'} \right), \quad (23)$$

where h_0^{tw-s} , h_0^{tw-tw} , c_3 , and c_4 are model-specific fitting parameters. Shear on each slip system evolves at a rate of

$$\dot{\gamma}^\alpha = (1 - f_{tw}^{tot}) \dot{\gamma}_0^\alpha \left| \frac{\tau}{\xi^\alpha} \right|^m \operatorname{sgn}(\tau^\alpha). \quad (24)$$

where slip due to mechanical twinning accounting for the unidirectional character of twin formation is computed slightly differently,

$$\dot{\gamma} = (1 - f_{tw}^{tot}) \dot{\gamma}_0 \left| \frac{\tau}{\xi} \right|^m \mathcal{H}(\tau), \quad (25)$$

where \mathcal{H} is the Heaviside step function. The total twin volume is calculated as

$$f_{tw}^{tot} = \max \left(1.0, \sum_{\beta=1}^{N_{tw}} \frac{\gamma^\beta}{\gamma_{char}^\beta} \right), \quad (26)$$

where γ_{char} is the characteristic shear due to mechanical twinning and depends on the twin system. Interested readers are referred to Section 6 in [6] for a comprehensive context of constitutive models in CPFEM.

4 Materials constitutive model calibration workflow

4.1 A seamless integration for optimizer and forward simulations

Figure 2 shows a seamless integration workflow for coupling the asynchronous parallel Bayesian optimization algorithm with an integrated forward ICME modules, composed of DREAM.3D [81] and DAMASK [6] with PETSc [82] as the spectral solver [83]. The integration between DREAM.3D and DAMASK has been demonstrated in the past by Diehl et al. [84]. A similar variant of `aphB0-2GP-3B0` is implemented and publicly available in DAKOTA [85].

4.2 Microstructure-ensemble average loss function

In this paper, the loss function, to be minimized, is modeled as

$$\mathcal{L}_{\text{loss}} = \frac{\left[\int (\sigma_{\text{comp}}(\varepsilon) - \sigma_{\text{exp}}(\varepsilon))^2 d\varepsilon \right]^{1/2}}{\min(\varepsilon_{\text{comp}}, \varepsilon_{\text{exp}})}, \quad (27)$$

where $\varepsilon_{\text{comp}}$ and σ_{comp} are computational results from CPFEM simulation, respectively, and ε_{exp} and σ_{exp} are experimental results from experimental data, respectively. The computational stress used is from the Cauchy stress tensor, and the computational strain used is the true logarithmic strain.

We measure the loss function in L_2 norm, normalized by the observable minimum strain ε to promote fitting over a wide range of strain ε . Due to the relatively high failure strain, CPFEM occasionally would fail before reaching the ultimate yield strain and therefore, the computational stress-strain curve is only compared on a much shorter computational strain interval compared to the experimental strain interval. To ensure that a fair comparison between early terminated CPFEM simulations and normal CPFEM simulations, we penalize the loss by dividing the normal L_2 loss by the $\min(\varepsilon_{\text{comp}}, \varepsilon_{\text{exp}})$, which is always less than or equal to ε_{exp} . We interpolate the numerical and experimental stress-strain equivalent curve using a cubic spline to accurately approximate the L_2 loss function. Gaussian filter is sometimes applied to remove noises from the experimental data. Eisenlohr et al. [83] and Shanthraj et al. [86] demonstrated that using the spectral solver, it is possible to achieve a fairly accurate homogenized stress-strain curve with relatively low-resolution mesh. This observation subsequently justifies the usage of low-resolution mesh in our approach. The Matérn-1/2 kernel, which corresponds to the exponential kernel (and the Brownian motion – [55, pp 85–86]), is used in GP to model and overfit the loss function.

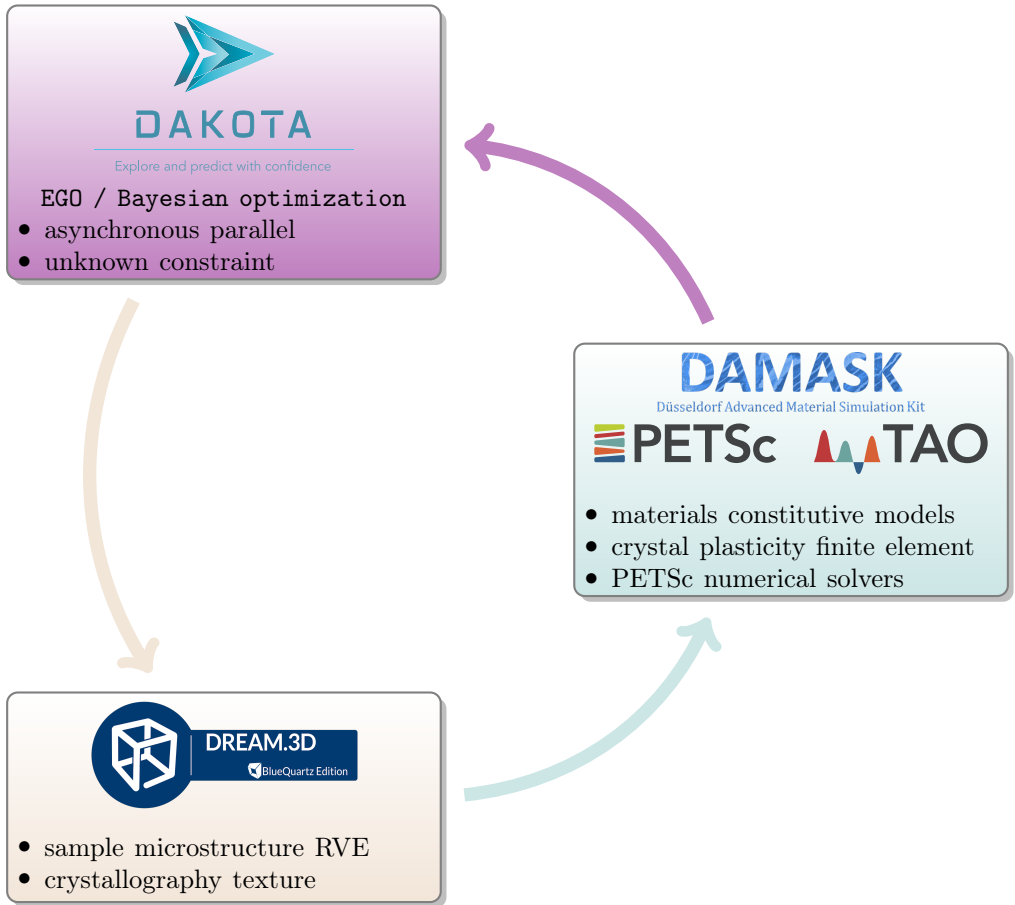


Fig. 2: An asynchronous parallel model calibration workflow for CPFEM. The workflow is mainly controlled by an advanced Bayesian optimization algorithm, called **aphB0-2GP-3B0**, to schedule an iteration on a high-performance computer. Each iteration is composed of a parameterized set of constitutive model parameters, obtained from the Bayesian optimizer. The parameterized input is then parsed into DAMASK input files. DREAM.3D is invoked to generate an ensemble of microstructure RVEs. With the complete inputs, the average loss function is evaluated and returned to the Bayesian optimizer. Iterations are scheduled asynchronously so that multiple iterations can run concurrently on a supercomputing platform to minimize the wall-clock waiting time.

5 Case study 1: Stainless steel 304L

5.1 Design of numerical experiment

The average equiaxed grain size is set as $8.0\mu\text{m}$, following Wang et al. [87] with random crystallographic texture due to the lack of experimental data [88]. Elastic constants are adopted from Lu et al. [89] and tabulated in Table 2; face-centered cubic (fcc) system is assumed. Using DREAM.3D, a RVE of $80\mu\text{m} \times 80\mu\text{m} \times 80\mu\text{m}$ is constructed and down-sampled to $8 \times 8 \times 8$ mesh. A uniaxial loading condition is imposed on the RVE with $\dot{F}_{11} = 10^{-3}\text{s}$. At every time, concurrently, 10 CPFEM simulations are performed, under the batch settings of (6,4,0) in the `aphB0-2GP-3B` asynchronous parallel BO algorithm [42], with a batch size of 6 dedicated to the acquisition batch and a batch size of 4 dedicated to the exploration batch. The 5-dimensional input for each run \mathbf{x} is the set of phenomenological constitutive model parameters $(\tau_0, \tau_\infty, h_0, n, a)$, with the lower bounds of [1 MPa, 100 MPa, 100 MPa, 1.2, 1] and the upper bounds of [150 MPa, 12,000 MPa, 10,000 MPa, 150, 25], respectively. The reference shear rate $\dot{\gamma}_0$ is fixed at 0.001 s^{-1} .

Table 2: Elastic constants for SS304L [87].

Elastic constants	Units	Value
C_{11}	GPa	262.2
C_{12}	GPa	112.0
C_{44}	GPa	74.6

5.2 Comparison between fitted constitutive model and experimental data

Table 3: Fitted phenomenological constitutive model parameters for SS304L.

Variable	Description	Units	Value
$\dot{\gamma}_0$	reference shear rate	s^{-1}	0.001
τ_0	slip resistance	MPa	90
τ_∞	saturation stress	MPa	7295.1754
h_0	slip hardening parameter	MPa	392.9772
n	strain rate sensitivity parameter	–	120
a	slip hardening parameter	–	8.0

Table 3 lists the optimal phenomenological constitutive model parameters used for SS304L in this study, which is found after 352 iterations. Figure 3 presents the comparison between the CPFEM numerical results with optimized constitutive model parameters and the experimental data, where the aleatory uncertainty in RVE instantiation and epistemic uncertainty in mesh resolution are both quantified. The  blue shaded region captures the uncertainty due

to both aleatory and epistemic uncertainty in the optimization process. An ensemble of 4 RVEs are also shown in Figure 3 as ●, ●, ●, ●, to highlight the natural variability and inherent randomness of microstructures on the σ/ε curves. Overall, the phenomenological constitutive model without twinning fits well in the high-strain ($\varepsilon > 0.10$) plasticity regime but does not accurately capture the hardening behaviors. The low-strain ($\varepsilon < 0.10$) plasticity regime is poorly captured, due to the lack of intricacy in the constitutive model.

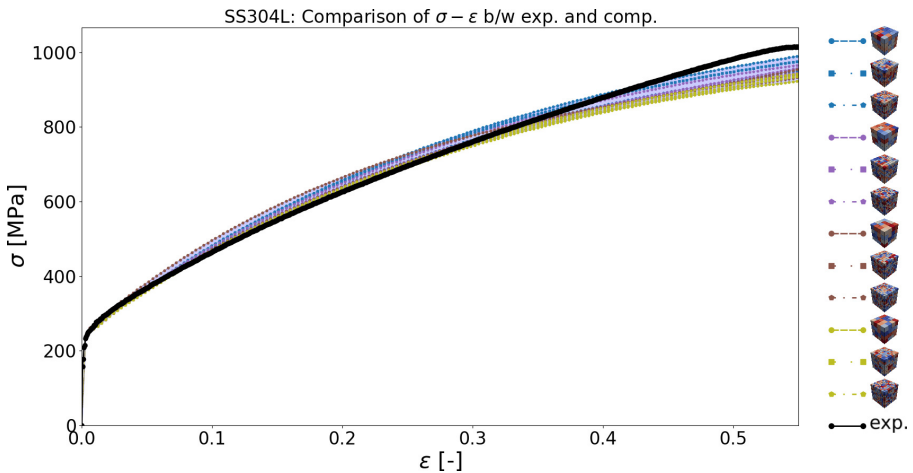


Fig. 3: Comparison of equivalent stress-strain curve between optimal numerical results and experimental data for SS304L, where the constitutive model parameters used are tabulated in Table 3. ● denotes experimental data. σ/ε associated with RVE 1 is shown as ●. σ/ε associated with RVE 2 is shown as ●. σ/ε associated with RVE 3 is shown as ●. σ/ε associated with RVE 4 is shown as ●. The material variability is shown as the □ shaded region. Readers are referred to the color version online.

6 Case study 2: Tantalum phenomenological constitutive model

6.1 Design of numerical experiment

In this case study, we are interested in fitting the bcc Tantalum, with the average grain size of $50\mu\text{m}$. Elastic constants are adopted from [90, 91] and tabulated in Table 4; body-centered cubic (bcc) system is assumed. Using DREAM.3D, a RVE of $80\mu\text{m} \times 80\mu\text{m} \times 80\mu\text{m}$ is constructed and down-sampled to $8 \times 8 \times 8$ mesh. A uniaxial loading condition is imposed on the RVE with $\dot{F}_{11} = 10^{-3}\text{s}$. No twinning is considered for quasi-static loading at the ambient temperature. Even though not considered in this study of calibrating phenomenological constitutive models, calculating Peierls stresses

in tantalum have been performed in the past through molecular dynamics simulation [92, 93]. The 5-dimensional input for each run \mathbf{x} is the set of phenomenological constitutive model parameters $(\tau_0, \tau_\infty, h_0, n, a)$, with the lower bounds of [1 MPa, 1 MPa, 1 MPa, 1.2, 1] and the upper bounds of [1,000 MPa, 10,000 MPa, 10,000 MPa, 150, 200], respectively. The reference shear rate $\dot{\gamma}_0$ is fixed at 0.001 s^{-1} . At every time, concurrently, 24 CPFEM simulations are performed, under the batch settings of (10,10,4) in the `aphB0-2GP-3B` asynchronous parallel Bayesian optimization algorithm [42], with a batch size of 10 dedicated to the acquisition batch, a batch size of 4 dedicated to the objective exploration batch, and a batch size of 4 dedicated to the classification exploration batch.

Table 4: Elastic constants for Tantalum [90, 91].

Elastic constants	Units	Value
C_{11}	GPa	267
C_{12}	GPa	161
C_{44}	GPa	82.5

6.2 Comparison between fitted constitutive model and experimental data

Table 5: Fitted phenomenological constitutive model parameters for Tantalum.

Variable	Description	Units	Value
$\dot{\gamma}_0$	reference shear rate	s^{-1}	0.001
τ_0	slip resistance	MPa	67.4641
τ_∞	saturation stress	MPa	7295.1754
h_0	slip hardening parameter	MPa	1959.1320
n	strain rate sensitivity parameter	–	45.2726
a	slip hardening parameter	–	200.0

Table 5 lists the optimal phenomenological constitutive model parameters used for Tantalum in this study, which is found after 1135 iterations. Figure 4 presents the comparison between the CPFEM numerical results with optimized constitutive model parameters and the experimental data, where the aleatory uncertainty in RVE instantiation and epistemic uncertainty in mesh resolution are both quantified. The  blue shaded region captures the uncertainty due to both aleatory and epistemic uncertainty in the optimization process. An ensemble of 4 RVEs are also shown in Figure 4 as , , , , to highlight the natural variability and inherent randomness of microstructures on the σ/ε curves. Overall, the numerical results agree relatively well with the experimental data, given a long interval of strain, except for the immediate drop in stress

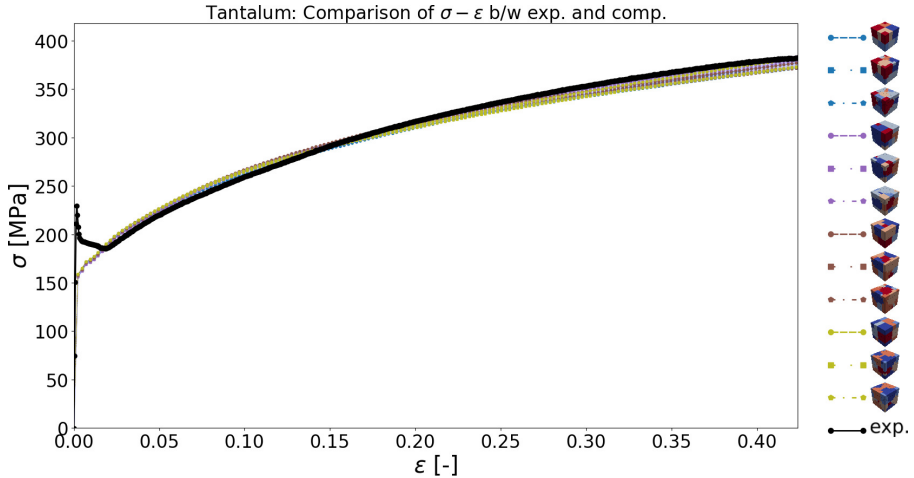


Fig. 4: Comparison of equivalent stress-strain curve between optimal numerical results and experimental data for Tantalum, where the constitutive model parameters used are tabulated in Table 5. ● denotes experimental data. σ/ε associated with RVE 1 is shown as ●. σ/ε associated with RVE 2 is shown as ●. σ/ε associated with RVE 3 is shown as ●. σ/ε associated with RVE 4 is shown as ●. The material variability is shown as the □ shaded region. Readers are referred to the color version online.

right after the elastic deformation. It should be noted that the experimental data are filtered to exclude the peak and this immediate sharp drop; in other words, we exclude the data between the strain $\varepsilon = [9.3667 \cdot 10^{-4}, 1.8572 \cdot 10^{-2}]$.

7 Case study 3: Cantor CrMnFeCoNi high-entropy alloy phenomenological constitutive model

7.1 Design of numerical experiment

Table 6: Elastic constants for Cantor alloy [94, 95].

Elastic constants	Units	Value
C_{11}	GPa	172
C_{12}	GPa	108
C_{44}	GPa	92

In this case study, we are interested in fitting a simple phenomenological constitutive model without twinning for the Cantor alloy, which is also known as the CrMnFeCoNi high-entropy alloy. The experimental data is obtained

from Chen et al [96]. We follow [94, 95] for elastic constants, which are tabulated in Table 6. Only fcc system is considered in this case study, even though fcc, hcp (hexagonal closed packed) [96], and bcc [97] phases are observed experimentally. Using DREAM.3D, a RVE of $80\mu\text{m} \times 80\mu\text{m} \times 80\mu\text{m}$ is constructed and down-sampled to $8 \times 8 \times 8$ mesh. A uniaxial loading condition is imposed on the RVE with $\dot{F}_{11} = 10^{-3}$ s. Average grain size of $7\mu\text{m}$ from literature [98–100]. No twinning is considered in fitting the phenomenological constitutive model. At every time, concurrently, 24 CPFEM simulations are performed, under the batch settings of (10,10,0) in the aphB0-2GP-3B asynchronous parallel Bayesian optimization algorithm [42], with a batch size of 10 dedicated to the acquisition batch, a batch size of 10 dedicated to the objective exploration batch. The 5-dimensional input for each run \mathbf{x} is the set of phenomenological constitutive model parameters $(\tau_0, \tau_\infty, h_0, n, a)$.

7.2 Comparison between fitted constitutive model and experimental data

Table 7: Fitted phenomenological constitutive model parameters for Cantor alloy (without twinning).

Variable	Description	Units	Value
$\dot{\gamma}_0$	reference shear rate	s^{-1}	0.001
τ_0	slip resistance	MPa	1.0
τ_∞	saturation stress	MPa	10000.0
h_0	slip hardening parameter	MPa	1959.1320
n	strain rate sensitivity parameter	–	41.2673
a	slip hardening parameter	–	128.3608

Table 7 lists the optimal phenomenological constitutive model parameters used for the Cantor alloy in this study, which is found after 969 iterations. Figure 5 presents the comparison between the CPFEM numerical results with optimized constitutive model parameters and the experimental data, where the aleatory uncertainty in RVE instantiation and epistemic uncertainty in mesh resolution are both quantified. The  blue shaded region captures the uncertainty due to both aleatory and epistemic uncertainty in the optimization process. An ensemble of 4 RVEs are also shown in Figure 5 as , , , , to highlight the natural variability and inherent randomness of microstructures on the σ/ε curves. Uncertainty quantification on constitutive models in CPFEM has been carried out in the past [101]. However, it seems that the phenomenological constitutive model without twinning in this case study is inadequate to model the complex materials behaviors of the Cantor alloy, which suggests a more complicated dislocation-density-based constitutive, e.g. [102], may better fit its behaviors over a wide range of compositions and temperature.

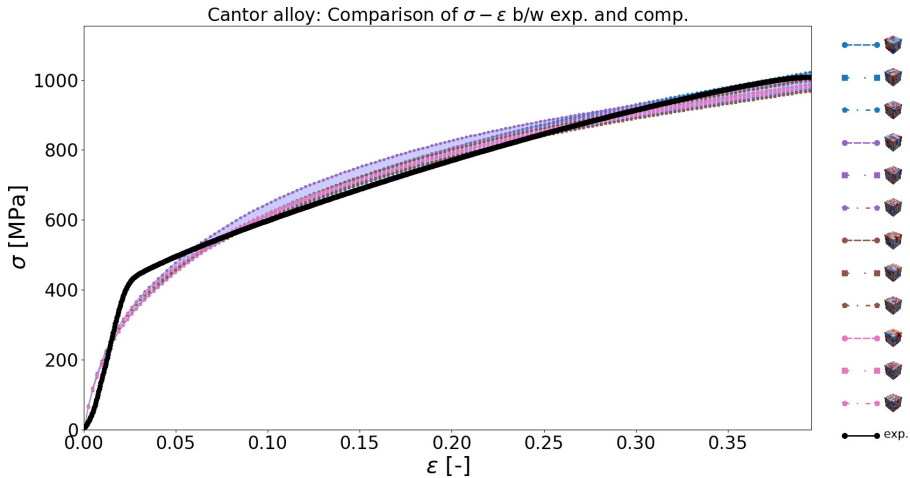


Fig. 5: Comparison of equivalent stress-strain curve between optimal numerical results and experimental data for Cantor alloy, where the constitutive model parameters used are tabulated in Table 7. ● denotes experimental data [96]. σ/ε associated with RVE 1 is shown as ●. σ/ε associated with RVE 2 is shown as ●. σ/ε associated with RVE 3 is shown as ●. σ/ε associated with RVE 4 is shown as ●. The material variability is shown as the shaded region. Readers are referred to the color version online.

8 Discussion & Conclusion

In this paper, we apply an asynchronous parallel constrained BO algorithm [42] to calibrate phenomenological constitutive model for fcc SS304L, bcc Tantalum, and fcc Cantor alloy. To maximize the acquisition function, we rely on the CMA-ES algorithms [103–105], which is also gradient-free to search for the next most informative input parameters. Compared to other sequential optimization algorithms used in the literature, the **aphBO-2GP-3B** algorithm exploits the computational resource by *two* layers of parallelisms: the *optimization parallelism* and the *message passing interface (MPI) parallelism*, where the former takes a priority over the later due to diminishing return by Amdahl’s law [7].

Model calibration methods are mainly divided into two classes: deterministic and statistical [85]. On one hand, the deterministic model calibration seeks a unique set of parameters that optimally matches experimental data, where optimality is typically measured in L_2 , as done in this paper. On the other hand, the statistical model calibration, such as Bayesian inference [106], seeks a statistical characterization of parameters that are most consistent with the data. In this study, the only constraint is unknown, where the CPFEM simulation may not return a numerical value, e.g. NaN. This behavior occasionally happens, depending on the user-defined optimization bounds. This type of

constraints (i.e. blind constraints) is conveniently handled thanks to the internal binary classifier that penalize the acquisition function [42] to navigate the complex acquisition function map.

Multi-fidelity GP [107, 108] could also be used to combine the computational and experimental data, either at the same length-scale or in multi-scale manner [109]. In this study, we fix the mesh size due to its insensitivity, based on prior DAMASK studies, e.g. [83]. However, generalizing to an asynchronous parallel constrained multi-fidelity GP/BO framework with adaptive coarse and fine meshes is also possible and makes more sense, thus remaining as an interesting future research direction. In this study, the only constraint is unknown, where the CPFEM simulation may not return a numerical value, e.g. NaN. This behavior occasionally happens, depending on the user-defined optimization bounds. This type of constraints (i.e. blind constraints) is conveniently handled thanks to the internal binary classifier that penalize the acquisition function [42] to navigate the complex acquisition function map.

Based on the optimized constitutive model parameters, we conduct a simple verification and validation study to investigate the effects of aleatory uncertainty from random RVEs and epistemic uncertainty from mesh-resolution. The homogenized computational results are shown to be reproducibly consistent with the experimental data. Stainless steel 304L and Tantalum results show an excellent fit without twinning; however, Cantor alloy results shows a relatively poor fit due to an overly simplified constitutive model for a complex materials system.

We conclude that the asynchronous parallel constrained BO [42] is capable of calibrating phenomenological constitutive models for CPFEM, which paves way for further research in the future.

Acknowledgment

The views expressed in the article do not necessarily represent the views of the U.S. Department of Energy or the United States Government. Sandia National Laboratories is a multimission laboratory managed and operated by National Technology and Engineering Solutions of Sandia, LLC., a wholly owned subsidiary of Honeywell International, Inc., for the U.S. Department of Energy's National Nuclear Security Administration under contract DE-NA-0003525.

A.T. thanks Prof. Robert O. Ritchie (University of Berkeley / Lawrence Berkeley National Laboratory) and Prof. Bernd Gludovatz (University of New South Wales) for sharing their Cantor alloys experimental data, Prof. Philip Eisenlohr (Michigan State University) and Dr. Pieterjan Robbe (Sandia National Laboratories) for numerous fruitful discussions.

The authors are extremely grateful to the editors and the two anonymous reviewers for their valuable comments and suggestions, which have greatly improved the quality of our manuscript.

References

- [1] Hey, T., Tansley, S., Tolle, K.M., *et al.*: The Fourth Paradigm: Data-intensive Scientific Discovery vol. 1. Microsoft research Redmond, WA, ??? (2009)
- [2] Agrawal, A., Choudhary, A.: Perspective: Materials informatics and big data: Realization of the “fourth paradigm” of science in materials science. *APL Materials* **4**(5), 053208 (2016)
- [3] US NSTC: Materials Genome Initiative for Global Competitiveness. Executive Office of the President, National Science and Technology Council, ??? (2011)
- [4] Holdren, J.P., Kalil, T., Wadia, C., Locascio, L., Kung, H., Horton, L., Warren, J.: Materials genome initiative strategic plan (2014). National Science And Technology Council (2014)
- [5] Lander, E., Koizumi, K., Christodoulou, J., Sapochak, L., Friedersdorf, L.E., Warren, J.: Materials genome initiative strategic plan (2021). National Science And Technology Council (2021)
- [6] Roters, F., Diehl, M., Shanthraj, P., Eisenlohr, P., Reuber, C., Wong, S.L., Maiti, T., Ebrahimi, A., Hochrainer, T., Fabritius, H.-O., *et al.*: DAMASK–The Düsseldorf Advanced Material Simulation Kit for modeling multi-physics crystal plasticity, thermal, and damage phenomena from the single crystal up to the component scale. *Computational Materials Science* **158**, 420–478 (2019)
- [7] Hill, M.D., Marty, M.R.: Amdahl’s law in the multicore era. *Computer* **41**(7), 33–38 (2008)
- [8] Raabe, D.: Computational Materials Science: the Simulation of Materials Microstructures and Properties. Wiley-Vch, ??? (1998)
- [9] Raabe, D., Roters, F., Barlat, F., Chen, L.-Q.: Continuum Scale Simulation of Engineering Materials: Fundamentals-microstructures-process Applications. John Wiley & Sons, ??? (2004)
- [10] Janssens, K.G.F., Raabe, D., Kozeschnik, E., Miodownik, M.A., Nestler, B.: Computational Materials Engineering: an Introduction to Microstructure Evolution. Academic Press, ??? (2010)
- [11] Roters, F., Eisenlohr, P., Bieler, T.R., Raabe, D.: Crystal Plasticity Finite Element Methods: in Materials Science and Engineering. John Wiley & Sons, ??? (2011)

- [12] Chakraborty, A., Eisenlohr, P.: Evaluation of an inverse methodology for estimating constitutive parameters in face-centered cubic materials from single crystal indentations. *European Journal of Mechanics-A/Solids* **66**, 114–124 (2017)
- [13] Hérault, D., Thuillier, S., Lee, S.-Y., Manach, P.-Y., Barlat, F.: Calibration of a strain path change model for a dual phase steel. *International Journal of Mechanical Sciences* **194**, 106217 (2021)
- [14] Nguyen, T., Francom, D.C., Luscher, D.J., Wilkerson, J.: Bayesian calibration of a physics-based crystal plasticity and damage model. *Journal of the Mechanics and Physics of Solids* **149**, 104284 (2021)
- [15] Savage, D.J., Feng, Z., Knezevic, M.: Identification of crystal plasticity model parameters by multi-objective optimization integrating microstructural evolution and mechanical data. *Computer Methods in Applied Mechanics and Engineering* **379**, 113747 (2021)
- [16] Hochhalter, J., Bomarito, G., Yeratapally, S., Leser, P., Ruggles, T., Warner, J., Leser, W.: Non-deterministic calibration of crystal plasticity model parameters. In: *Integrated Computational Materials Engineering (ICME)*, pp. 165–198. Springer, ??? (2020)
- [17] Kuhn, J., Spitz, J., Sonnweber-Ribic, P., Schneider, M., Böhlke, T.: Identifying material parameters in crystal plasticity by Bayesian optimization. *Optimization and Engineering* **23**(3), 1489–1523 (2022)
- [18] Sedighiani, K., Diehl, M., Traka, K., Roters, F., Sietsma, J., Raabe, D.: An efficient and robust approach to determine material parameters of crystal plasticity constitutive laws from macro-scale stress–strain curves. *International Journal of Plasticity* **134**, 102779 (2020)
- [19] Sedighiani, K., Traka, K., Roters, F., Raabe, D., Sietsma, J., Diehl, M.: Determination and analysis of the constitutive parameters of temperature-dependent dislocation-density-based crystal plasticity models. *Mechanics of Materials* **164**, 104117 (2022)
- [20] Wang, K., Sun, W., Salager, S., Na, S., Khaddour, G.: Identifying material parameters for a micro-polar plasticity model via X-ray micro-computed tomographic (CT) images: lessons learned from the curve-fitting exercises. *International Journal for Multiscale Computational Engineering* **14**(4) (2016)
- [21] Liu, Y., Sun, W., Fish, J.: Determining material parameters for critical state plasticity models based on multilevel extended digital database. *Journal of Applied Mechanics* **83**(1) (2016)

- [22] Herrera-Solaz, V., LLorca, J., Dogan, E., Karaman, I., Segurado, J.: An inverse optimization strategy to determine single crystal mechanical behavior from polycrystal tests: Application to AZ31 Mg alloy. *International Journal of Plasticity* **57**, 1–15 (2014)
- [23] Do, B., Ohsaki, M.: Bayesian optimization for inverse identification of cyclic constitutive law of structural steels from cyclic structural tests. In: *Structures*, vol. 38, pp. 1079–1097 (2022). Elsevier
- [24] Do, B., Ohsaki, M.: Proximal-exploration multi-objective bayesian optimization for inverse identification of cyclic constitutive law of structural steels. *Structural and Multidisciplinary Optimization* **65**(7), 1–24 (2022)
- [25] Seidl, D.T., Granzow, B.N.: Calibration of elastoplastic constitutive model parameters from full-field data with automatic differentiation-based sensitivities. *International Journal for Numerical Methods in Engineering* **123**(1), 69–100 (2022)
- [26] Corona, E., Kramer, S.L.B., Scherzinger, W.M., Jones, A.R.: Anisotropic plasticity model forms for extruded Al 7079: Part I, calibration. *International Journal of Solids and Structures* **213**, 135–147 (2021)
- [27] Jones, E., Corona, E., Jones, A.R., Scherzinger, W.M., Kramer, S.L.B.: Anisotropic plasticity model forms for extruded Al 7079: Part II, validation. *International Journal of Solids and Structures* **213**, 148–166 (2021)
- [28] Karandikar, J., Chaudhuri, A., No, T., Smith, S., Schmitz, T.: Bayesian optimization for inverse calibration of expensive computer models: A case study for Johnson-Cook model in machining. *Manufacturing Letters* **32**, 32–38 (2022)
- [29] Sun, X., Wang, H.: A method for crystal plasticity model parameter calibration based on Bayesian optimization. In: *Magnesium Technology 2022*, pp. 105–111. Springer, ??? (2022)
- [30] Morand, L., Helm, D.: A mixture of experts approach to handle ambiguities in parameter identification problems in material modeling. *Computational Materials Science* **167**, 85–91 (2019)
- [31] Generale, A.P., Hall, R., Brockman, R., Joseph, V.R., Jefferson, G., Zawada, L., Pierce, J., Kalidindi, S.R.: Bayesian calibration of continuum damage model parameters for an oxide-oxide ceramic matrix composite using inhomogeneous experimental data. *Mechanics of Materials*, 104487 (2022)
- [32] Zambaldi, C., Yang, Y., Bieler, T.R., Raabe, D.: Orientation informed

nanoindentation of α -Titanium: Indentation pileup in hexagonal metals deforming by prismatic slip. *Journal of Materials Research* **27**(1), 356–367 (2012)

- [33] Bolzon, G., Maier, G., Panico, M.: Material model calibration by indentation, imprint mapping and inverse analysis. *International Journal of Solids and Structures* **41**(11-12), 2957–2975 (2004)
- [34] Fuhg, J.N., van Wees, L., Obstalecki, M., Shade, P., Bouklas, N., Kase-mer, M.: Machine-learning convex and texture-dependent macroscopic yield from crystal plasticity simulations. *Materialia* **23**, 101446 (2022)
- [35] Fuhg, J.N., Marino, M., Bouklas, N.: Local approximate Gaussian process regression for data-driven constitutive models: development and comparison with neural networks. *Computer Methods in Applied Mechanics and Engineering* **388**, 114217 (2022)
- [36] Zhang, T., Xie, H., Huo, M., Jia, F., Li, L., Pan, D., Wu, H., Liu, J., Yang, T., Jiang, F., *et al.*: A method for the determination of individual phase properties in multiphase steels. *Materials Science and Engineering: A* **854**, 143707 (2022)
- [37] Foumani, Z.Z., Shishehbor, M., Yousefpour, A., Bostanabad, R.: Multi-fidelity cost-aware bayesian optimization. *arXiv preprint arXiv:2211.02732* (2022)
- [38] Wang, J., Clark, S.C., Liu, E., Frazier, P.I.: Parallel bayesian global optimization of expensive functions. *Operations Research* **68**(6), 1850–1865 (2020)
- [39] Veasna, K., Feng, Z., Zhang, Q., Knezevic, M.: Machine learning-based multi-objective optimization for efficient identification of crystal plasticity model parameters. *Computer Methods in Applied Mechanics and Engineering* **403**, 115740 (2023)
- [40] Ponweiser, W., Wagner, T., Biermann, D., Vincze, M.: Multiobjective optimization on a limited budget of evaluations using model-assisted \mathcal{S} -metric selection. In: *Parallel Problem Solving from Nature–PPSN X: 10th International Conference, Dortmund, Germany, September 13-17, 2008*. *Proceedings 10*, pp. 784–794 (2008). Springer
- [41] Bostanabad, R., Kearney, T., Tao, S., Apley, D.W., Chen, W.: Leveraging the nugget parameter for efficient Gaussian process modeling. *International journal for numerical methods in engineering* **114**(5), 501–516 (2018)
- [42] Tran, A., Eldred, M., Wildey, T., McCann, S., Sun, J., Visintainer, R.J.:

- aphBO-2GP-3B: a budgeted asynchronous parallel multi-acquisition functions for constrained Bayesian optimization on high-performing computing architecture. *Structural and Multidisciplinary Optimization* **65**(4), 1–45 (2022)
- [43] Brochu, E., Hoffman, M.W., de Freitas, N.: Portfolio allocation for Bayesian optimization. arXiv preprint arXiv:1009.5419 (2010)
- [44] Brochu, E., Cora, V.M., de Freitas, N.: A tutorial on Bayesian optimization of expensive cost functions, with application to active user modeling and hierarchical reinforcement learning. arXiv preprint arXiv:1012.2599 (2010)
- [45] Shahriari, B., Swersky, K., Wang, Z., Adams, R.P., de Freitas, N.: Taking the human out of the loop: A review of Bayesian optimization. *Proceedings of the IEEE* **104**(1), 148–175 (2016)
- [46] Frazier, P.I.: A tutorial on Bayesian optimization. arXiv preprint arXiv:1807.02811 (2018)
- [47] Jones, D.R., Schonlau, M., Welch, W.J.: Efficient global optimization of expensive black-box functions. *Journal of Global Optimization* **13**(4), 455–492 (1998)
- [48] Tran, A., Wildey, T., McCann, S.: sMF-BO-2CoGP: A sequential multi-fidelity constrained Bayesian optimization for design applications. *Journal of Computing and Information Science in Engineering* **20**(3), 1–15 (2020)
- [49] Tran, A., Wang, Y., Furlan, J., Pagalthivarthi, K.V., Garman, M., Cutright, A., Visintainer, R.J.: WearGP: A UQ/ML wear prediction framework for slurry pump impellers and casings. In: *ASME 2020 Fluids Engineering Division Summer Meeting* (2020). American Society of Mechanical Engineers
- [50] Tran, A., Wildey, T., McCann, S.: sBF-BO-2CoGP: A sequential bi-fidelity constrained Bayesian optimization for design applications. In: *Proceedings of the ASME 2019 IDETC/CIE. International Design Engineering Technical Conferences and Computers and Information in Engineering Conference*, vol. Volume 1: 39th Computers and Information in Engineering Conference (2019). American Society of Mechanical Engineers. V001T02A073
- [51] Tran, A., Sun, J., Furlan, J.M., Pagalthivarthi, K.V., Visintainer, R.J., Wang, Y.: pBO-2GP-3B: A batch parallel known/unknown constrained Bayesian optimization with feasibility classification and its applications in computational fluid dynamics. *Computer Methods in Applied*

Mechanics and Engineering **347**, 827–852 (2019)

- [52] Tran, A., Tran, M., Wang, Y.: Constrained mixed-integer Gaussian mixture Bayesian optimization and its applications in designing fractal and auxetic metamaterials. *Structural and Multidisciplinary Optimization* **59**, 2131–2154 (2019)
- [53] Tran, A., He, L., Wang, Y.: An efficient first-principles saddle point searching method based on distributed kriging metamodels. *ASCE-ASME Journal of Risk and Uncertainty in Engineering Systems, Part B: Mechanical Engineering* **4**(1), 011006 (2018)
- [54] Tran, A., Furlan, J.M., Pagalthivarthi, K.V., Visintainer, R.J., Wildey, T., Wang, Y.: WearGP: A computationally efficient machine learning framework for local erosive wear predictions via nodal Gaussian processes. *Wear* **422**, 9–26 (2019)
- [55] Rasmussen, C.E.: *Gaussian Processes in Machine Learning*. MIT Press, ??? (2006)
- [56] Lee, J., Bahri, Y., Novak, R., Schoenholz, S.S., Pennington, J., Sohl-Dickstein, J.: Deep neural networks as Gaussian processes. In: *ICLR* (2018)
- [57] Garriga-Alonso, A., Rasmussen, C.E., Aitchison, L.: Deep convolutional networks as shallow Gaussian processes. In: *ICLR* (2019)
- [58] Kushner, H.J.: A new method of locating the maximum point of an arbitrary multipeak curve in the presence of noise. *Journal of Basic Engineering* **86**(1), 97–106 (1964)
- [59] Mockus, J.: On Bayesian methods for seeking the extremum. In: *Optimization Techniques IFIP Technical Conference*, pp. 400–404 (1975). Springer
- [60] Mockus, J.: The Bayesian approach to global optimization. *System Modeling and Optimization*, 473–481 (1982)
- [61] Jones, D.R.: A taxonomy of global optimization methods based on response surfaces. *Journal of global optimization* **21**(4), 345–383 (2001)
- [62] Bull, A.D.: Convergence rates of efficient global optimization algorithms. *Journal of Machine Learning Research* **12**(Oct), 2879–2904 (2011)
- [63] Snoek, J., Larochelle, H., Adams, R.P.: Practical Bayesian optimization of machine learning algorithms. In: *Advances in Neural Information Processing Systems*, pp. 2951–2959 (2012)

- [64] Scott, W., Frazier, P., Powell, W.: The correlated knowledge gradient for simulation optimization of continuous parameters using Gaussian process regression. *SIAM Journal on Optimization* **21**(3), 996–1026 (2011)
- [65] Auer, P.: Using confidence bounds for exploitation-exploration trade-offs. *Journal of Machine Learning Research* **3**(Nov), 397–422 (2002)
- [66] Srinivas, N., Krause, A., Kakade, S.M., Seeger, M.: Gaussian process optimization in the bandit setting: No regret and experimental design. arXiv preprint arXiv:0912.3995 (2009)
- [67] Srinivas, N., Krause, A., Kakade, S.M., Seeger, M.W.: Information-theoretic regret bounds for Gaussian process optimization in the bandit setting. *IEEE Transactions on Information Theory* **58**(5), 3250–3265 (2012)
- [68] Daniel, C., Viering, M., Metz, J., Kroemer, O., Peters, J.: Active reward learning. In: *Robotics: Science and Systems* (2014)
- [69] Hernández-Lobato, J.M., Hoffman, M.W., Ghahramani, Z.: Predictive entropy search for efficient global optimization of black-box functions. In: *Advances in Neural Information Processing Systems*, pp. 918–926 (2014)
- [70] Hernández-Lobato, J.M., Gelbart, M., Hoffman, M., Adams, R., Ghahramani, Z.: Predictive entropy search for Bayesian optimization with unknown constraints. In: *International Conference on Machine Learning*, pp. 1699–1707 (2015)
- [71] Hernández-Lobato, D., Hernández-Lobato, J., Shah, A., Adams, R.: Predictive entropy search for multi-objective Bayesian optimization. In: *International Conference on Machine Learning*, pp. 1492–1501 (2016)
- [72] Hernández-Lobato, J.M., Gelbart, M.A., Adams, R.P., Hoffman, M.W., Ghahramani, Z.: A general framework for constrained bayesian optimization using information-based search. *Journal of Machine Learning Research* (2016)
- [73] Hennig, P., Schuler, C.J.: Entropy search for information-efficient global optimization. *Journal of Machine Learning Research* **13**(Jun), 1809–1837 (2012)
- [74] Wang, Z., Jegelka, S.: Max-value entropy search for efficient Bayesian optimization. arXiv preprint arXiv:1703.01968 (2017)
- [75] Wilson, J., Hutter, F., Deisenroth, M.: Maximizing acquisition functions for Bayesian optimization. *Advances in Neural Information Processing Systems* **31**, 9884–9895 (2018)

- [76] Parr, J., Keane, A., Forrester, A.I., Holden, C.: Infill sampling criteria for surrogate-based optimization with constraint handling. *Engineering Optimization* **44**(10), 1147–1166 (2012)
- [77] Digabel, S.L., Wild, S.M.: A taxonomy of constraints in simulation-based optimization. arXiv preprint arXiv:1505.07881 (2015)
- [78] Hoffman, M., Brochu, E., de Freitas, N.: Portfolio allocation for bayesian optimization. In: *Proceedings of the Twenty-Seventh Conference on Uncertainty in Artificial Intelligence. UAI'11*, pp. 327–336. AUAI Press, Arlington, Virginia, USA (2011)
- [79] Hutchinson, J.W.: Bounds and self-consistent estimates for creep of polycrystalline materials. *Proceedings of the Royal Society of London. A. Mathematical and Physical Sciences* **348**(1652), 101–127 (1976)
- [80] Kalidindi, S.R.: Incorporation of deformation twinning in crystal plasticity models. *Journal of the Mechanics and Physics of Solids* **46**(2), 267–290 (1998)
- [81] Groeber, M.A., Jackson, M.A.: DREAM.3D: a digital representation environment for the analysis of microstructure in 3D. *Integrating materials and manufacturing innovation* **3**(1), 5 (2014)
- [82] Balay, S., Abhyankar, S., Adams, M., Brown, J., Brune, P., Buschelman, K., Dalcin, L., Dener, A., Eijkhout, V., Gropp, W., et al.: *PETSc users manual* (2019)
- [83] Eisenlohr, P., Diehl, M., Lebensohn, R.A., Roters, F.: A spectral method solution to crystal elasto-viscoplasticity at finite strains. *International Journal of Plasticity* **46**, 37–53 (2013)
- [84] Diehl, M., Groeber, M., Haase, C., Molodov, D.A., Roters, F., Raabe, D.: Identifying structure–property relationships through DREAM.3D representative volume elements and DAMASK crystal plasticity simulations: An integrated computational materials engineering approach. *JOM* **69**(5), 848–855 (2017)
- [85] Dalbey, K., Eldred, M., Geraci, G., Jakeman, J., Maupin, K., Mon-schke, J.A., Seidl, D., Tran, A., Menhorn, F., Zeng, X.: *Dakota, A Multilevel Parallel Object-Oriented Framework for Design Optimization, Parameter Estimation, Uncertainty Quantification, and Sensitivity Analysis: Version 6.16 Theory Manual*. Technical report, Sandia National Lab.(SNL-NM), Albuquerque, NM (United States) (2022)
- [86] Shanthraj, P., Diehl, M., Eisenlohr, P., Roters, F., Raabe, D., Chen, C., Chawla, K., Chawla, N., Chen, W., Kagawa, Y.: Spectral solvers for

- crystal plasticity and multi-physics simulations. Handbook of Mechanics of Materials, Springer, Berlin, 978–981 (2019)
- [87] Wang, Y., Sun, D., Bai, Y., Pang, Z.: Study on grain size control technology of 304L austenitic stainless steel. In: Journal of Physics: Conference Series, vol. 2045, p. 012023 (2021). IOP Publishing
- [88] Hamza, S., Boumerzoug, Z., Helbert, A.-L., Bresset, F., Baudin, T.: Texture analysis of welded 304L pipeline steel. Journal of Metals, Materials and Minerals **29**(3) (2019)
- [89] Lu, J., Becker, A., Sun, W., Tanner, D.: Simulation of cyclic plastic behavior of 304L steel using the crystal plasticity finite element method. Procedia materials science **3**, 135–140 (2014)
- [90] Lim, H., Carroll, J., Battaile, C.C., Buchheit, T., Boyce, B., Weinberger, C.: Grain-scale experimental validation of crystal plasticity finite element simulations of tantalum oligocrystals. International Journal of Plasticity **60**, 1–18 (2014)
- [91] Duesbery, M.a.-S., Vitek, V.: Plastic anisotropy in bcc transition metals. Acta Materialia **46**(5), 1481–1492 (1998)
- [92] Wang, G., Strachan, A., Çağın, T., GoddardIII, W.A.: Calculating the Peierls energy and Peierls stress from atomistic simulations of screw dislocation dynamics: application to bcc tantalum. Modelling and Simulation in Materials Science and Engineering **12**(4), 371 (2004)
- [93] Anglade, P.-M., Jomard, G., Robert, G., Zerah, G.: Computation of the Peierls stress in tantalum with an extended-range modified embedded atom method potential. Journal of Physics: Condensed Matter **17**(12), 2003 (2005)
- [94] Gludovatz, B., George, E.P., Ritchie, R.O.: Processing, microstructure and mechanical properties of the CrMnFeCoNi high-entropy alloy. JOM **67**(10), 2262–2270 (2015)
- [95] Laplanche, G., Gadaud, P., Bärsch, C., Demtröder, K., Reinhart, C., Schreuer, J., George, E.: Elastic moduli and thermal expansion coefficients of medium-entropy subsystems of the CrMnFeCoNi high-entropy alloy. Journal of Alloys and Compounds **746**, 244–255 (2018)
- [96] Chen, S., Oh, H.S., Gludovatz, B., Kim, S.J., Park, E.S., Zhang, Z., Ritchie, R.O., Yu, Q.: Real-time observations of TRIP-induced ultrahigh strain hardening in a dual-phase CrMnFeCoNi high-entropy alloy. Nature communications **11**(1), 1–8 (2020)

- [97] Zeng, Z., Xiang, M., Zhang, D., Shi, J., Wang, W., Tang, X., Tang, W., Wang, Y., Ma, X., Chen, Z., *et al.*: Mechanical properties of Cantor alloys driven by additional elements: A review. *Journal of Materials Research and Technology* **15**, 1920–1934 (2021)
- [98] Thurston, K.V., Gludovatz, B., Hohenwarter, A., Laplanche, G., George, E.P., Ritchie, R.O.: Effect of temperature on the fatigue-crack growth behavior of the high-entropy alloy crmnfeconi. *Intermetallics* **88**, 65–72 (2017)
- [99] Chen, S., Tseng, K.-K., Tong, Y., Li, W., Tsai, C.-W., Yeh, J.-W., Liaw, P.K.: Grain growth and Hall-Petch relationship in a refractory HfNbTaZrTi high-entropy alloy. *Journal of Alloys and Compounds* **795**, 19–26 (2019)
- [100] Rackwitz, J., Yu, Q., Yang, Y., Laplanche, G., George, E.P., Minor, A.M., Ritchie, R.O.: Effects of cryogenic temperature and grain size on fatigue-crack propagation in the medium-entropy CrCoNi alloy. *Acta Materialia* **200**, 351–365 (2020)
- [101] Tran, A., Wildey, T., Lim, H.: Microstructure-sensitive uncertainty quantification for crystal plasticity finite element constitutive models using stochastic collocation method. *Frontiers in Materials* **9**, 1–20 (2022)
- [102] Steinmetz, D.R., Jäpel, T., Wietbrock, B., Eisenlohr, P., Gutierrez-Urrutia, I., Saeed-Akbari, A., Hickel, T., Roters, F., Raabe, D.: Revealing the strain-hardening behavior of twinning-induced plasticity steels: Theory, simulations, experiments. *Acta Materialia* **61**(2), 494–510 (2013)
- [103] Hansen, N., Ostermeier, A.: Completely derandomized self-adaptation in evolution strategies. *Evolutionary computation* **9**(2), 159–195 (2001)
- [104] Hansen, N., Müller, S.D., Koumoutsakos, P.: Reducing the time complexity of the derandomized evolution strategy with covariance matrix adaptation (CMA-ES). *Evolutionary computation* **11**(1), 1–18 (2003)
- [105] Hansen, N., Kern, S.: Evaluating the CMA evolution strategy on multimodal test functions. In: *International Conference on Parallel Problem Solving from Nature*, pp. 282–291 (2004). Springer
- [106] Zhang, W., Bostanabad, R., Liang, B., Su, X., Zeng, D., Bessa, M.A., Wang, Y., Chen, W., Cao, J.: A numerical Bayesian-calibrated characterization method for multiscale prepreg preforming simulations with tension-shear coupling. *Composites Science and Technology* **170**, 15–24 (2019)

- [107] Kennedy, M.C., O'Hagan, A.: Predicting the output from a complex computer code when fast approximations are available. *Biometrika* **87**(1), 1–13 (2000)
- [108] Kennedy, M.C., O'Hagan, A.: Bayesian calibration of computer models. *Journal of the Royal Statistical Society: Series B (Statistical Methodology)* **63**(3), 425–464 (2001)
- [109] Tran, A., Tranchida, J., Wildey, T., Thompson, A.P.: Multi-fidelity machine-learning with uncertainty quantification and Bayesian optimization for materials design: Application to ternary random alloys. *The Journal of Chemical Physics* **153**, 074705 (2020)